Fluorescence Modulation of *ortho*-Green Fluorescent Protein Chromophores following Ultrafast Proton Transfer in Solution

Sean A. Boulanger,[1] Cheng Chen,[1] Ivan N. Myasnyanko,[2,3] Mikhail S. Baranov,[2,3] and Chong Fang*[,1]

[1]Department of Chemistry, Oregon State University, 153 Gilbert Hall, Corvallis, Oregon 97331, United States

[2]Institute of Bioorganic Chemistry, Russian Academy of Sciences, Miklukho-Maklaya 16/10, Moscow 117997, Russia

[3]Pirogov Russian National Research Medical University, Ostrovitianov 1, Moscow 117997, Russia

*Corresponding author email: Chong.Fang@oregonstate.edu (Chong Fang)

Abstract

Photophysical and photochemical properties of the green fluorescent protein (GFP) chromophore and derivatives are the foundation for their broad and diverse bioimaging applications. To date, ultrafast spectroscopic tools represent the key for unravelling the fluorescence mechanisms toward rational design of this powerful biomimetic framework. To correlate a fundamental reaction, excited-state intramolecular proton transfer (ESIPT), with the chromophore emission properties, we implement experimental and computational toolsets to elucidate the real-time electronic and structural dynamics of two archetypal *ortho*-GFP chromophores (*o*-HBDI and *o*-LHBDI) both possessing an intramolecular hydrogen bond to undergo efficient ESIPT, only differing in a bridge-bond constraint. Using excited-state femtosecond stimulated Raman spectroscopy (FSRS), a low-frequency phenolic (P)-ring-deformation mode (~562 cm^{-1}) was uncovered to accompany ESIPT. The tautomerized chromophore undergoes either rapid isomerization about P ring to reach the ground state with essentially no fluorescence for *o*-HBDI, or enhanced (up to an impressive 180-fold in acetonitrile) and solvent-polarity-dependent fluorescence by conformationally locking the P ring in *o*-LHBDI. The uncovered significant dependence of fluorescence enhancement ratio on solvent viscosity confirms P-ring isomerization as the dominant nonradiative decay pathway for *o*-HBDI. This work provides crucial insights into the dynamic solute-solvent electrostatic and steric interactions, thereby enabling the application-specific improvement of ESIPT-capable molecules as versatile fluorescence-based sensors and imaging agents from large Stokes shift emission to brighter probes in physiological environments.

1. Introduction

Proton transfer is among the most abundant and fundamental processes in organic, inorganic, and biological systems,[1-10] which can occur between molecules and solvents (intermolecular) leading to a change of the protonation state, or within the molecule itself (intramolecular) resulting in the formation of a constitutional (structural) isomer. Excited-state proton transfer (ESPT) and excited-state intramolecular proton transfer (ESIPT) represent functional processes with distinct underlying mechanisms that have powered broad applications from research labs to industrial settings and from biological to energy fields, which include bioimaging and materials advances.[9,11] Recently, there have been extensive studies into the potential of ESIPT reactions from optoelectronic devices, fluorescence sensors, organic light-emitting diodes, lasers, optical data storages to displays, amongst others.[9,12-15] Many of the molecules possessing ESPT or ESIPT capabilities are naturally occurring, such as the green fluorescent protein (GFP) from *Aequorea victoria*,[16,17] a blue-green pigment xylindein from fungi *Chlorociboria aeruginosa*,[18] and a red pigment Draconin red from fungi *Scytalidium cuboideum*.[19] The fundamental knowledge and insights obtained that delineate the proton transfer mechanisms in various natural systems have since inspired rational design inquiries and targeted molecular engineering endeavors.

Fluorescent proteins, for example, may be too large for certain applications from transmitting through the blood-brain barrier to the accurate measurement of inter-chromophore distance, whereas synthetic chromophore analogues can be much better suited due to their smaller sizes; however, these "bare" chromophores pose an intrinsic issue. The fluorescence quantum yield (FQY) is often diminished outside the protein matrix due to an altered electrostatic environment, thus promoting additional nonradiative decay pathways and possibly leading to a twisted intramolecular charge transfer (TICT) state as seen in the synthetic GFP chromophore, (*Z*)-5-(4-

hydroxybenzylidene)-2,3-dimethyl-3,5-dihydro-4*H*-imidazol-4-one (*p*-HBDI), in solution.[20-22] In addition to a high FQY value, a large Stokes shift and red emission are also desirable for bioimaging in living systems. The recently termed "double-donor-one-acceptor" model based on *p*-HBDI derivatives has been demonstrated to red-shift the emission, enhance the Stokes shift through ESPT, and increase the FQY through conformational locking of the chromophore in solution, all without drastically increasing the molecular size by extending the π-conjugation.[23]

Notably, ESIPT occurs through an intramolecular hydrogen (H)-bond between the donor (e.g., –OH, –SH, $–NH_2$, –NHR) and acceptor (e.g., –C=O, –C=S, –N=) moieties in a conjugated molecule.[9,11,12,14] This process could result in dual fluorescence from the excited states of normal (N*) and tautomer (T*) forms or single fluorescence from the T* form, a large Stokes shift (~10,000 cm^{-1}), and an ultrafast ESIPT rate ($k_{ESIPT} > 10^{12}$ s^{-1}). ESIPT thus provides an alternative approach to traditional intermolecular ESPT methodologies for designing molecules with suitable bioimaging properties. For example, a prototypical ESIPT system can be strategically tuned to alter k_{ESIPT} and to either promote or inhibit N*-form emission, as was the case in altering the acidity of an amine group in the N–H-type ESIPT systems and the phenolic-ring hydroxy group in GFP chromophore analogues.[11,24,25] The typically ultrafast ESIPT rate can be reduced in systems with an N–H···N hydrogen bond, as shown in a synthesized blue fluorescent protein analogue due to its weakened intramolecular H-bond compared to O and S's stronger H-bond donating and accepting capabilities.[11,26] k_{ESIPT} can also be tuned by a substituent to either raise or lower the ESIPT energy barrier,[11,24,25] or enhance intramolecular charge transfer (ICT) to perturb ESIPT by reducing the acidity of proton donor and give rise to a charge-transfer emission band[9,27] that has been shown to be tunable.[6,28,29] Since ESIPT emission is highly sensitive to the environment, a comprehensive solvent-dependent study is warranted.

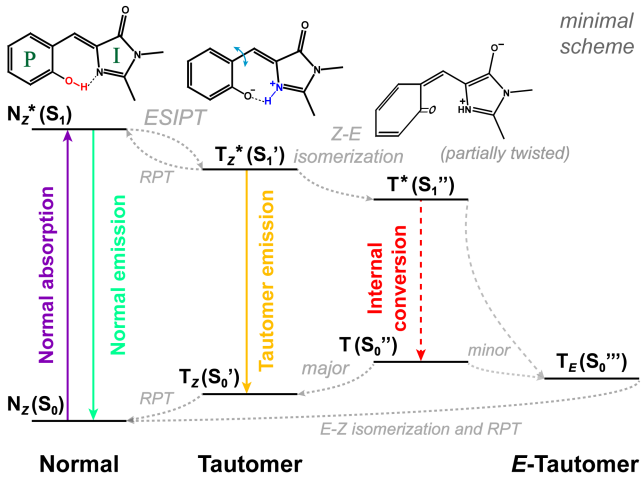

Scheme 1. Schematic of a typical ESIPT photocycle that undergoes *Z*-*E* (*cis*-*trans*) photoisomerization. See main text for an enriched photocycle with intermediate electronic states for *o*-HBDI and *o*-LHBDI. The representative chemical structures of *o*-HBDI are shown in the upper panel along the excited-state reaction coordinate. RPT, reverse proton transfer.

Scheme 1 summarizes typical processes in an ESIPT-capable system that also undergoes *Z*-*E* or *cis*-*trans* photoisomerization like in GFP chromophore structural isomers, (*Z*)-5-(2-hydroxybenzylidene)-2,3-dimethyl-3,5-dihydro-4*H*-imidazol-4-one (*o*-HBDI) and its phenolic-ring-locked derivative (*Z*)-5-(7-hydroxy-2,3-dihydro-1*H*-inden-1-ylidene)-2,3-dimethyl-3,5-dihydro-4*H*-imidazol-4-one (*o*-LHBDI) (Scheme 2), which are the focus of this work. ESIPT reactions have been characterized by steady-state electronic spectroscopy, quantum calculations, and ultrafast electronic techniques including femtosecond (fs) fluorescence upconversion, picosecond-nanosecond (ps-ns) time-correlated single photon counting, time-resolved fluorescence, and fs transient absorption (fs-TA).[13,24,30] However, a plethora of information regarding the ESIPT photocycle remains forfeited by neglecting structural effects in both the ground and excited states, or certain local environments.

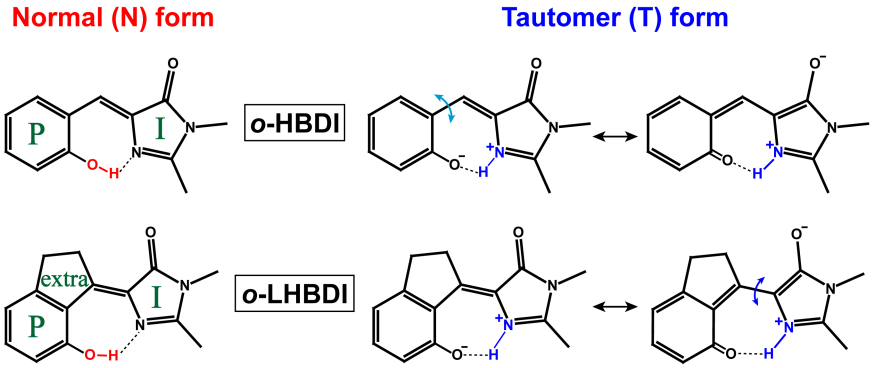

Scheme 2. Chemical structures of the neutral normal (N; red) and zwitterionic tautomer (T; blue) forms of *o*-HBDI and *o*-LHBDI. Solid lines represent covalent bonds while dashed lines represent intramolecular hydrogen bonds. Three rings (P, I, and extra) of the chromophore framework are denoted. Two resonance structures of the T form are shown, along with representative P- and I-ring twists in the double-headed cyan and blue arrows, respectively, for *o*-HBDI and *o*-LHBDI.

Herein, we employ steady-state electronic spectroscopy, fs-TA, ground- and excited-state femtosecond stimulated Raman spectroscopy (FSRS), and quantum calculations to elucidate the ESIPT reaction mechanism of two GFP-derived chromophores that possess a seven-membered-ring with an intramolecular hydrogen bond (*o*-HBDI and *o*-LHBDI, see Scheme 2). By studying the correlated electronic and vibrational features, we can obtain deeper insights into these key contrasting functional molecules. We strategically chose solvents with various electrostatic and steric properties ranging from polar protic (methanol: MeOH) and aprotic (acetonitrile and dichloromethane: ACN and DCM) to largely nonpolar aprotic (toluene: Tol) to examine effects of solvent properties on the competing excited-state radiative and nonradiative relaxation pathways. We observed ultrafast (<100 fs) ESIPT reaction in all solvents, accompanied by a ~562 cm^{-1} P-ring-deformation motion that can modulate the O–H···N distance. The excited-state potential energy surface (PES) manifests ICT characters, while the isomerization energy barriers and FQY values are both solvent-polarity dependent, which increase as the solvent polarity decreases.[31] The

fundamental knowledge obtained in both the electronic and vibrational domains for *ortho*-GFP chromophores provides rational design principles of ESIPT-capable molecules with suitable and tunable properties for broad applications in bioimaging, optoelectronics, life and photosciences.

2. Results and Discussion

2.1. Steady-State Electronic Spectroscopy Establishes the Foundation for Photoinduced Properties. It is well-known that the GFP chromophore fluorescence is quenched in solution due to ultrafast nonradiative *cis-trans* isomerization.[22,32,33] Successful restoration of the fluorescence in *p*-HBDI involved conformational locking of the methine bridge between the phenolic (P) and imidazolinone (I) rings using a Zn^{2+} ion or $–BF_2$ group.[34,35] Although the electronic and vibrational properties of *p*-HBDI change upon moving the hydroxy group to *ortho* position in *o*-HBDI, further locking of P ring in *o*-LHBDI can provide a contrasting system to shed important light on the dominant isomerization pathway, and subsequent FQY, of this ESIPT-capable molecule. Herein, the ground-state (excited-state) normal and tautomer forms are denoted as N (N*) and T (T*).

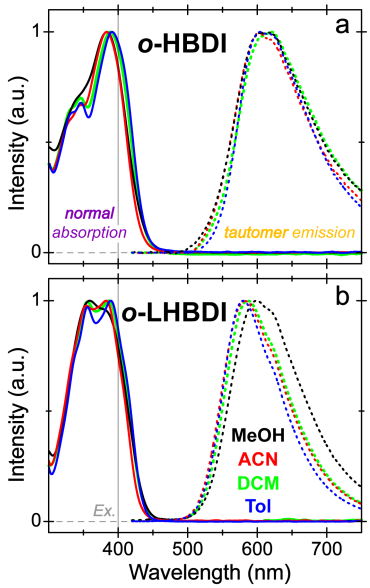

Figure 1. Steady-state electronic characterization of the neutral (a) *o*-HBDI and (b) *o*-LHBDI in solution. The normal-form absorption (solid lines) and tautomer-form emission spectra (dotted

lines) are color-coded according to solvents (MeOH, black; ACN, red; DCM, green; and Tol, blue). The actinic pump for fs-TA and excited-state FSRS experiments was tuned to be near the normal-form absorption peak at 400 nm (vertical gray line; *Ex.*, excitation).

The absorption and emission spectra of the neutral *o*-HBDI and *o*-LHBDI in MeOH, ACN, DCM, and Tol (Figure 1, see data summary in Table 1) display interesting patterns that allow for intriguing comparisons between the two chromophores in various solvents. Although there are ESIPT-capable molecules with N and T configurations in the ground state, the energetically favored structure for both *ortho*-GFP chromophore analogues is the normal *cis*-form (Scheme 2, Figure S1). The N-form absorption of *o*-HBDI and *o*-LHBDI is largely conserved in solution, with the much less polar Tol leading to a red-shifted peak versus that in polar MeOH, ACN, and DCM solvents. The single-band emission from the tautomer form (T^*, see below) is conserved for *o*-HBDI,[13,24,30,36] likely due to a planar fluorescent state (FS) that is reached prior to solvation or isomerization events (Scheme 1), reminiscent of the unlocked *p*-HBDI derivatives.[21,22] The red-shifted absorption (by ~465 cm^{-1}) and conserved emission (within 55 cm^{-1}) peaks of *o*-HBDI from MeOH to Tol (Figure S2a,b) suggest a more polar ground state; however, the nature of fluorescent state requires time-resolved spectroscopy. Meanwhile, the red-shifted absorption (by ~675 cm^{-1}) and blue-shifted emission (by ~580 cm^{-1}) peaks of *o*-LHBDI from MeOH to Tol (Figure S2d,e) exhibit similar magnitudes of energy variation. This finding convolutes the interpretation whether the ground or excited state has higher polarity since the electron density distribution is swiftly altered upon photoexcitation and chromophore tautomerization in solution (Figure S3).

Interestingly, the redshift of ground-state absorption (GSA) energies of the *o*-HBDI partially twisted T-form in MeOH to Tol (Figure S2c) from time-resolved fs-TA measurements (see below) manifests a staggering energy difference of ~2580 cm^{-1} and allows for experimental validation

that the zwitterionic T-form is more polar than the neutral N-form, particularly in the electronic ground state. The overall large Stokes shift (~8400–9600 cm^{-1}) of *o*-HBDI and *o*-LHBDI is reminiscent of typical ESIPT systems,[9,12,14] while the smallest Stokes shift was observed in Tol solvent. Previous studies of a methylated *o*-HBDI (*o*-MBDI) compound, without a donatable proton, yielded no ESIPT and a typical modest Stokes shift supporting only N* emission.[30,36]

Table 1. Steady-state electronic spectral properties of *o*-HBDI and *o*-LHBDI in solution

Solvent	*o*-HBDI			*o*-LHBDI			Solvent parameters [a]		
	Abs./em. (nm) [b]	Stokes shift (cm^{-1}) [b]	FQY ($\times10^{-3}$) [c]	Abs./em. (nm) [b]	Stokes shift (cm^{-1}) [b]	FQY [c]	η	ε	E_T^N
MeOH	384/605	9513	0.24	380/599	9621	0.014	0.55	32.7	0.762
ACN	383/604	9553	0.51	383/582	8928	0.093	0.34	37.5	0.460
DCM	389/606	9205	1.0	387/585	8746	0.113	0.44	8.93	0.309
Toluene	391/603	8992	4.4	390/579	8370	0.214	0.59	2.38	0.099

[a] The selected solvent properties listed are viscosity (η) with centipoise (cP) unit, dielectric constant (ε), and normalized empirical polarity parameter (E_T^N).[37]

[b] Experimentally determined from steady-state electronic spectroscopy measurements. The neutral forms of *o*-HBDI and *o*-LHBDI were prepared in various solvents as listed.

[c] Determined upon 400 nm excitation of the neutral form. The relative method with coumarin 153 ($\lambda_{abs}/\lambda_{em}$ = 422/533 nm) as the standard was performed.

To confirm ESIPT with a single-band T* emission, we collected steady-state electronic spectra of neutral (in MeOH) and anionic (in MeOH + 1,8-diazabicyclo[5.4.0]undec-7-ene/DBU) *o*-HBDI (Figure S4). Anionic species are known to have a redder emission than neutral species due to the stabilization of S_1 state. The post-ESIPT zwitterionic *o*-HBDI has a more stabilized S_1 state than the anionic form, leading to a further red-shifted emission peak.[30,36] Moreover, the absorption and

emission of N and T* *o*-HBDI in MeOH from quantum calculations (see the SI Experimental Materials and Methods, and details after Figure S3 caption) support this assignment. The increased photoacidity of the P-ring hydroxy group of N* form promotes subsequent tautomerization and electron density redistribution to T* (Figure S3), thus leading to a large Stokes shift.[9,11,12] Together with the calculated natural bond orbital (NBO) charges on the P-ring O, I-ring N, and donatable H that support ESIPT (Table S1), the proton-transfer-coupled ICT is plausible for N*→T* and T→N tautomerization. It is likely that minimal ICT occurs from the N→N* transition as the hydroxy group has weak electron-donating property unless it becomes deprotonated, although the exact order of ultrafast processes has been debated.[29,38] In essence, quantum calculations confirm the experimental results where the zwitterionic T* form is electronically more favorable than the singly charged anionic form in the excited state (Figures 1 and S4).

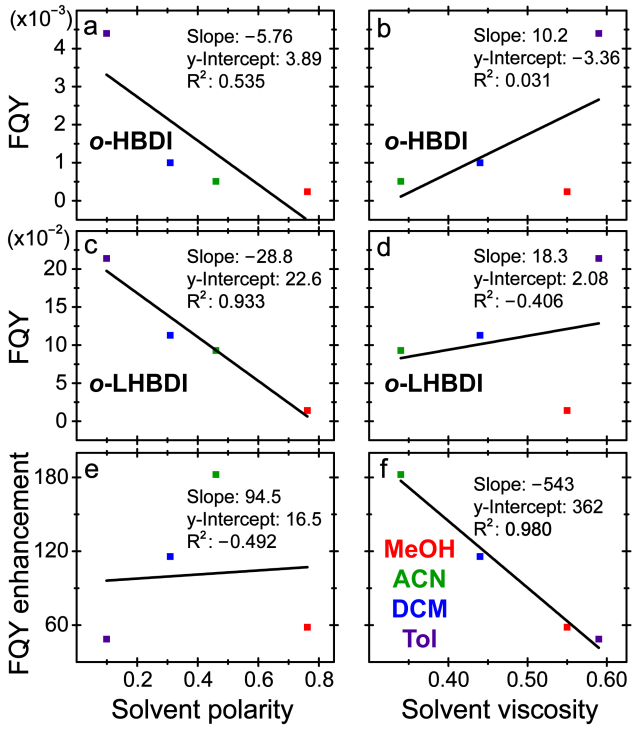

Figure 2. Correlations between the chromophore fluorescence properties and solvent parameters. Plots of *o*-HBDI and *o*-LHBDI FQY (a/b and c/d) and the FQY ratio of *o*-LHBDI over *o*-HBDI

(e/f) against solvent polarity/viscosity, respectively, are shown with linear regression fits (lines). Spectral data points (squares) are color-coded with respect to the solvents used (MeOH, red; ACN, green; DCM, blue; Tol, purple). R^2 values are listed, which can be negative when the selected model does not follow the data trend so the fit is worse than a horizontal line (see panels d and e).

Notably, the FQY increases in both *o*-HBDI and *o*-LHBDI as the solvent polarity and H-bond donating and accepting abilities decrease (Figure 2a,c), suggesting that solvent properties play a pivotal role in the excited-state PES (see below).[11,28] The FQY of the P-ring-H-bonded *o*-HBDI ($\sim 10^{-3}$) in aqueous solution is an order of magnitude greater than that of the deprotonated *p*-HBDI ($\sim 10^{-4}$),[22,34,39] owing to the seven-membered-ring intramolecular H-bond (Scheme 2) that partially inhibits isomerization.[36] The O–H···N bond strength is expected to further increase the FQY difference between *o*- and *p*-HBDI isomers as a decrease in solvent H-bond donating and accepting capabilities results in less competition between inter- and intramolecular H-bonding.[11,36,40] Nonetheless, the overall FQY of *o*-HBDI remains miniscule, whereas the P-ring locking exerts a drastic effect on the FQY of *o*-LHBDI in MeOH, ACN, DCM, and Tol displaying an increase of ~60, 180, 115, and 50-fold (Table 1). The FQY values and enhancement ratios were plotted against both solvent polarity and viscosity parameters (Figure 2), since only the solvent-viscosity dependence was reported on the FQY in *o*-HBDI using aprotic polar and nonpolar solvents.[30] In this work, we observed a clear solvent-polarity dependence on the FQY in both *o*-HBDI and *o*-LHBDI (Figure 2a and c), more significant for the latter. Interestingly, there is no solvent-polarity dependence on the FQY enhancement (Figure 2e); however, removal of the MeOH data points would provide a linear correlation. Our findings thus substantiate the necessary inclusion of a protic polar solvent to gain a more complete understanding for such chromophores; we caution that the spectral data plots in this work are not exhaustive with respect to all solvent parameters.

We also found a clear solvent-viscosity dependence of the FQY enhancement ratios (Figure 2f), but not on the FQY values of *o*-HBDI and *o*-LHBDI individually (Figure 2b and d). The removal of MeOH data points to produce a largely linear correlation (Figure 2b, d, and e) implies that the enhanced solvent H-bond donating and accepting capabilities play a competitive role between inter- and intramolecular H-bonding to control ESIPT and isomerization rate.[11,12,40] The substantial difference between *o*-HBDI and *o*-LHBDI stems from the removal of one of the isomerization coordinates (P ring) and isolation of the other (I ring), which alters the excited-state PES and nonradiative decay pathways (see Section 2.2). The newly identified linear correlation between the FQY enhancement ratio and solvent viscosity (including the MeOH data) confirms theoretical calculations that isomerization along the P-ring twisting coordinate (a one-bond flip with a large volume change) is the dominant, energetically favorable nonradiative pathway that leads to a conical intersection.[41,42] If it were otherwise (i.e., I-ring twist dominates the excited-state relaxation pathway), the P-ring locking in *o*-LHBDI would not cause a dramatic variation for the FQY enhancement ratios from *o*-HBDI in solvents with different viscosities (Table 1). Moreover, the notable FQY drop of both chromophores in MeOH versus other solvents (Figure 2b,d, red points) is effectively "canceled" in the FQY enhancement ratio of *o*-LHBDI over *o*-HBDI (Figure 2f), indicating that the extra effect caused by the H-bond donating and accepting abilities of MeOH on FQY is comparable between these two chromophores in terms of a linear plot against solvent viscosity. This photoinduced P-ring twisting coordinate of *o*-HBDI is different from the widely accepted model for *p*-HBDI wherein the I-ring isomerization is the dominant nonradiative pathway that quenches fluorescence,[21,22,42] inferring that position of the hydroxy group on the P ring intrinsically governs the electronic and vibrational properties in both the ground and excited states of GFP chromophore analogues.

2.2. Femtosecond Transient Absorption Maps the Photoexcited Electronic Potential Energy Landscape. Steady-state electronic spectroscopy only provides a sliver of information about the ESIPT mechanism. Therefore, fs-TA spectroscopy was implemented to delineate ESIPT and subsequent energy dissipation pathways responsible for FQY enhancement upon P-ring locking in *o*-LHBDI and map the altered electronic excited-state PES in solvents with varying polarity and viscosity. These new TA results in four solvents with various properties complement the reported fluorescence upconversion data on *o*-LHBDI (no MeOH solvent was used),[13] allowing deeper mechanistic insights into the excited-state processes. The 400 nm actinic pump was strategically selected to efficiently populate the N* excited state (S_1) while the magic-angle polarization with respect to the probe minimizes anisotropy effects (see Figure 1 and SI Experimental Materials and Methods section). The 2D-contour plots of *o*-HBDI (Figure 3a, c, e, g) and *o*-LHBDI (Figure 4a, c, e, g) in four representative solvents visually accentuate spectral differences in their excited-state PESs and lifetimes governing the change of fluorescence properties upon conformational locking of the P ring, correlating the targeted chemical modification with major functionality change. The target analysis results, in the context of existing knowledge in the field about these *ortho*-GFP chromophores, allowed us to obtain additional information about the effects of molecular engineering (e.g., P-ring locking) on the electronic PES and nonradiative excited-state energy relaxation pathways in competition with the radiative (e.g., fluorescence) events.

Glotaran software[43] was employed to deconvolute transient electronic features of overlapping N*, T*, and T bands observed using global and target analysis. Global analysis yields evolution-associated difference spectra (EADS) with a sequential model (Figure S5), but the resultant spectra are challenging to interpret due to the concurrent pathways, such as ESIPT, isomerization, and fluorescence. Target analysis yields the species-associated difference spectra (SADS) with a

branched kinetic scheme that accounts for multiple competing energy dissipation pathways.[35] Four major states (**1**–**4**, bolded) and their lifetimes were retrieved for both chromophores in four solvents (Figures 3, 4, and S5) which allow for a systematic assignment of excited-state processes, aided by the solvent-polarity-dependent plots of key time constants and interpretations (Figure S6).

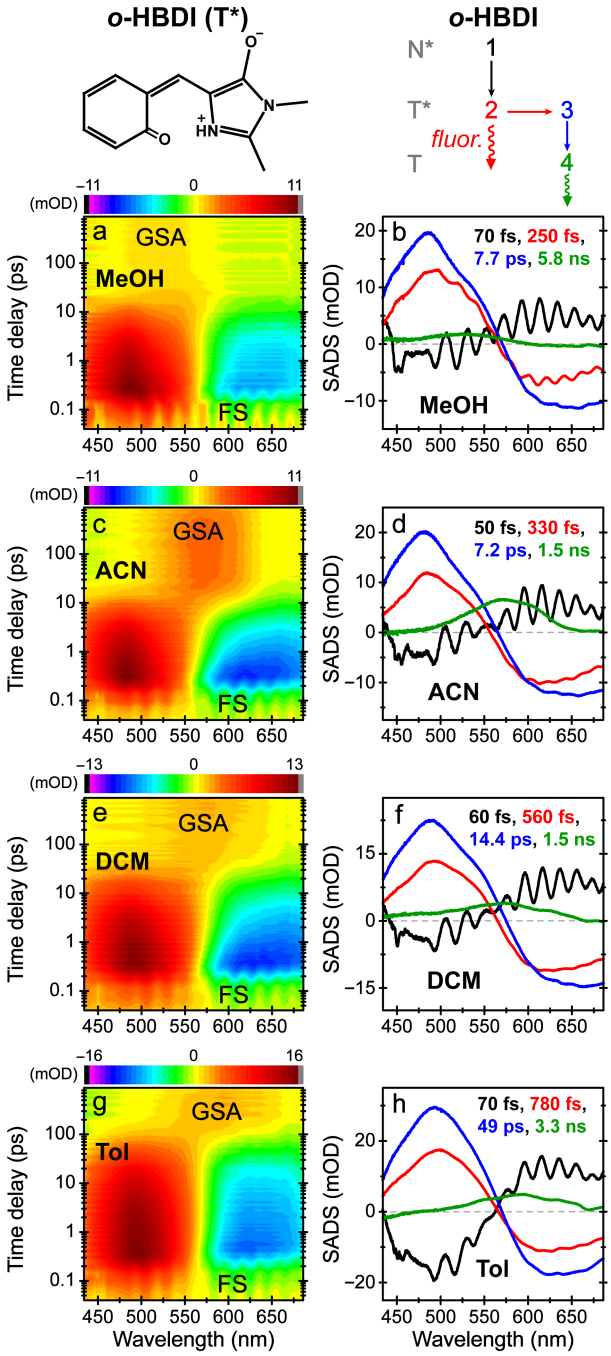

Figure 3. Ultrafast electronic dynamics of *o*-HBDI in solution. Chemical structure of the excited-state tautomer form (T*) is shown as the photoproduct after ultrafast ESIPT (<100 fs). Semilogarithmic contour plots of fs-TA spectra of *o*-HBDI in (a) MeOH, (c) ACN, (e) DCM, and (g) Tol after 400 nm excitation display clear excited-state absorption (positive) and stimulated emission (negative) bands denoted by the color bars. The fluorescent state (FS) and ground-state absorption (GSA) peak positions are labeled. From target analysis, the species-associated difference spectra (SADS, in milli-optical density/mOD unit) in each solvent are displayed in right panels (b), (d), (f), and (h) following the kinetic model displayed in the upper right corner. Straight and wavy arrows depict the electronic state transition and self-decay process, respectively. The retrieved lifetimes of four major states are color-coded (**1**, black; **2**, red; **3**, blue; and **4**, green) with a chosen equal branching ratio (50/50%) for **2** self-decay (*fluor.*) and **2**→**3** processes.

From the SADS of *o*-HBDI (Figure 3b, d, f, h), its N form is initially excited to N* (**1**) where ultrafast ESIPT (<100 fs) occurs to form a planar T* state (**2**) near the Franck-Condon region.[10,30] T* branches to either fluoresce (meaning state **2** is weakly emissive) or rapidly form a charge-separated (CS) state en route to a twisted intermediate tautomer state (TI*, **3**),[22,38] with an average fluorescent state lifetime with TI* formation on the ~250–780 fs timescale. The TI* undergoes further twisting over an energy barrier to internal conversion (or via a conical intersection) along the TICT(P) (see Section 2.1 above) isomerization coordinate on the ~7–49 ps timescale to form a ground state (**4**) twisted T-population. Such a notable change of time constants with respect to solvent properties, in conjunction with an uncovered effect on the FQY enhancement (Figure 2f), substantiates the assignment of this temporal component (**3**→**4** in kinetic scheme) along the *cis-trans* isomerization coordinate, likely via a dominant one-bond flip of P ring (see representative *o*-HBDI structures from T_Z^* to T^* states with an excited-state partial twist in Scheme 1).[30,41]

Importantly, we identified a linear relationship between the pertinent rate constants and solvent polarity (see Figure S6), but not viscosity, showing that the smaller solvent polarity lengthens the excited-state lifetimes of both states **2** and **3** (i.e., smallest/largest time constant in MeOH/Tol in Figure 3). In particular, the more prominent dependence of the sub-ps component (state **2** lifetime, see the correlation plot for *o*-HBDI in Figure S6a) on solvent polarity indicates that ICT plays a more important role en route to the chromophore ring-twisting events, tracked by state **3** lifetime (see the correlation plot for *o*-HBDI in Figure S6b). The miniscule FQYs of *o*-HBDI in various solvents (Table 1) support a dominant excited-state nonradiative decay pathway, reflected by the associated fs-TA dynamic features along the **2**→**3**→**4** route (see Figure 3 right panels, red→blue→green traces). In correlation with the reported ~5% *cis*-to-*trans* photoisomerization quantum yield,[30] most of the hot ground state species is an intermediate twisted *cis*-T through a conical intersection close to the *cis*-region:[38,41] the smaller-scale ring twists (~50°)[41] than those in *p*-HBDI (~90°)[21,22] are consistent with the aforementioned lack of dependence of excited-state rate constants on solvent viscosity. Post internal conversion/conical intersection,[38,41] the partially twisted *cis*-T form (e.g., state T(S_0'') in Scheme 1) relaxes back to the original *cis*-N form via reverse proton transfer (RPT, see Scheme 1) on the ns timescale in our fs-TA experiments (see Section 2.4 below), whereas the fully isomerized *trans*-T form was proposed to undergo deprotonation in ACN and return to the original *cis*-N form on the μs-to-ms timescale.[30]

Although the stimulated emission (SE) band of N* (see black traces in Figures 3 and S5) is near the calculated S_1 emission peak of ~490 nm,[13] the branched kinetic scheme provides deeper insights into reaction coordinates. Post ESIPT (**1**→**2** in kinetic scheme), the rapidly formed T* state exhibits an SE band position that is close to its steady-state emission peak (Figure 1a). Though the fluorescent state lifetimes increase with FQY values (Table 1) in both models, the intensity

(red traces, Figure 3) is lower than the TI* state (blue traces, Figure 3) in SADS. This is anticipated as the short-lived planar fluorescent state leads to the miniscule FQY of *o*-HBDI, whereas the nonradiative energy dissipation pathways (e.g., formation of CS and TI* states) are much more dominant. The expected redshift (blueshift) in the SE (ESA) band from the T* fluorescent state (**2**) to TI* state (**3**), clearly observed in SADS, denotes a more energetically stable CS state as ultrafast ICT occurs (Table S1) on the sub-ps timescale to accompany further P- and I-ring twisting motions, analogous to *p*-HBDI in solution.[22,44] It is notable that the use of target models does not change the kinetics of the fit versus lifetime analysis or a sequential model/EADS (Figure S5). Meanwhile, the intensity of the SADS component cannot be taken literally due to the chosen 50%/50% branching ratio that is representative not quantitative in nature, while the transition oscillator strength for each intermediate state (hence the peak amplitude and related population) is mostly unknown. Therefore, we primarily focused on the spectral shift (not the absolute peak amplitude change) between the retrieved components, such as state **2**→**3** for *o*-HBDI, with the pertinent ring-twisting motions affected by surrounding solvent molecules on ultrafast timescales.

The ground-state relaxation of a twisted T state (green traces, Figure 3) shows similar spectral features in both SADS and EADS since it is the last major process. The significant redshift of GSA band from polar to largely nonpolar solvents is in accord with the zwitterionic T-form having higher polarity than the neutral N-form, particularly in the ground state (Figure S2c). Also, the red-shifted T-form absorption peak (Figure 3) versus that of the N-form (Figure 1) is consistent with the P-ring twisted, energetically higher-lying T-form ground state configuration (e.g., see the T(S_0'') state in Scheme 1).[41] The ns time constants retrieved (Figure 3) are much shorter than previously reported,[30] so our fs-to-ns TA measurements likely track the electronic dynamics of the partially twisted *cis*-T form past the S_1/S_0 conical intersection (>95% population) and indicate that

different ground-state energy barriers for reverse proton transfer in various solvents play a role. For example, a larger barrier for *o*-HBDI in MeOH than Tol (Figure S1a) agrees with the trend for pertinent time constants (5.8 > 3.3 ns in Figure 3b,h). For the remaining <5% population that could reach the fully isomerized state (e.g., see the $T_E(S_0''')$ state in Scheme 1), time-resolved ns-to-μs experiments showed the ground state recovery of *o*-HBDI's *cis*-N form in ACN to be ~50 μs, attributed to the much slower proton recombination and *E*-*Z* isomerization after deprotonation of the minor *trans*-T species.[30]

For comparison, the locked *o*-LHBDI branched kinetic model and SADS (Figure 4b, d, f, and h) still show that N is initially excited to N* (**1**) with ultrafast ESIPT (<100 fs) to form T* (**2**), which branches to the isomerization route to form a TICT(I) dark state (**3**, in difference from the planar and emissive FS) or solvation route to reach a T* FS (**4**) on an average timescale of ~340–750 fs. Reminiscent of the aforementioned *o*-HBDI case, the retrieved two intermediate time constants do not match the typical solvation time (e.g., longitudinal relaxation time of ~5 ps for MeOH and ~0.2 ps for ACN, and Debye relaxation/principal dielectric relaxation time of ~50 ps for MeOH and ~1 ps for ACN), which indicates an ultrafast interplay between the chromophore electronic/structural dynamics and solvent motions. In particular, the dark state lifetime of ~15–70 ps for *o*-LHBDI is consistent with a more restrictive chromophore than *o*-HBDI (~7–49 ps, Figure 3) or *p*-HBDI (~2–3 ps),[22,30] substantiating a common assignment to ring-twisting motions in these GFP-chromophore isomers. As for the longest time constant, the planar T* FS (state **4**) lifetimes are ~270 ps (in MeOH) and 1.2 ns (in other solvents, Figure 4), which largely matches the reported population decay time constants of ~1.5–2.3 ns in ACN, DCM, and Tol from time-correlated single photon counting.[13] After the excited-state bifurcation from a planar T*, both the TICT(I) and T* FS relax back to the original N form through reverse proton transfer. The branched

kinetic scheme again demonstrates more meaningful insights into the electronic reaction coordinates (Figures 4 and S5), lending firm support to the multidimensional deactivation pathways for the photoexcited GFP chromophore derivatives in condensed phases.[10,13,22,42]

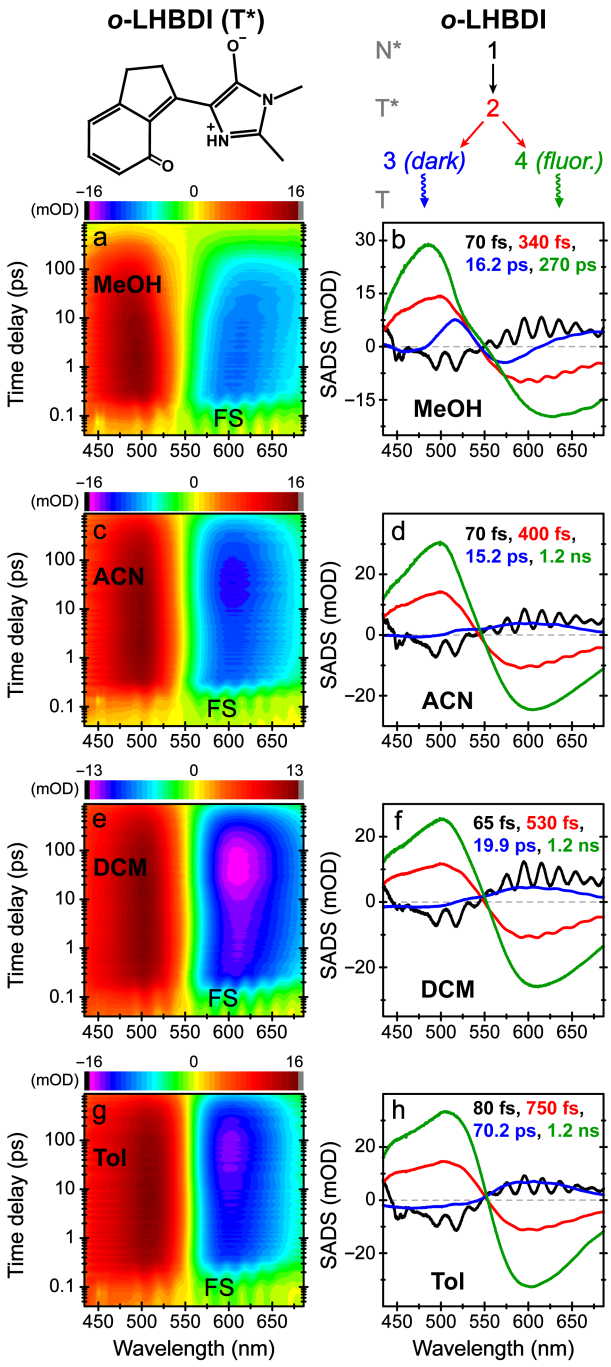

Figure 4. Ultrafast electronic dynamics of the locked *o*-HBDI derivative (*o*-LHBDI) in solution. Chemical structure of the excited-state tautomer form (T*) is shown as the photoproduct after

ultrafast ESIPT (<100 fs). Semilogarithmic contour plots of fs-TA spectra of *o*-LHBDI in (a) MeOH, (c) ACN, (e) DCM, and (g) Tol after 400 nm excitation show clear ESA (positive) and SE (negative) bands denoted by color bars. The fluorescent state (FS) peak positions are labeled. From target analysis, the species-associated difference spectra (SADS, in milli-optical density/mOD unit) in each solvent are displayed in right panels (b), (d), (f), and (h) with kinetic model displayed in the upper right corner. Straight and wavy arrows depict the electronic excited state transition and self-decay process, respectively. The retrieved lifetimes of four major states are color-coded (**1**, black; **2**, red; **3**, blue; and **4**, green) with a chosen equal branching ratio (50/50%) for **2**→**3** and **2**→**4** processes to highlight the spectral shift pattern.

As further proof for the ultrafast ESIPT reaction of *o*-LHBDI, the rapidly formed T* SE band position (red traces, Figure 4) largely matches its steady-state emission peak in each solvent (Figure 1b). Our model substantiates the rapid decay of this planar T* state (**2**), which could be a weakly emissive FS, along two competing pathways into a twisted dark state (**3**) and a further stabilized FS (**4**). The emissive step is accompanied by an SE peak redshift and a concomitant ESA peak blueshift to reach the solvated T* FS (green traces, Figure 4). Interestingly, a larger spectral shift occurs in polar solvents (see Figure 4 right panels, MeOH > ACN > DCM > Tol) as they effectively reorient to stabilize the highly polar, zwitterionic chromophore. We note that SADS account for the solvated T* FS feature with an intensity increase from T* state, while EADS yield similar intensities due to spectral convolution and a poor kinetic model (Figure S5 right panels).

Meanwhile, along the other relaxation pathway (**2**→**3** in kinetic scheme, Figure 4), the SE band for TICT(I) dark state peaks near 575 nm in MeOH (blue trace, Figure 4b), but cannot be observed in the other solvents (blue traces, Figure 4d, f, and h). This SE band may shift out of the spectral window as the solvent H-bond donating and accepting properties change, populating the trapped

species in a less relaxed dark state that becomes more inaccessible for the lower-polarity solvents exhibiting higher FQYs.[11,31] This dark state may also have an extremely weak SE transition oscillator strength, so the spectral overlap with an adjacent stronger ESA band yields an overall positive band. The retrieval of state **3** for *o*-LHBDI (blue traces in Figure 4) with different spectral profiles but lengthened (1.4–2.1 fold) lifetimes versus state **3** for *o*-HBDI (blue traces in Figure 3) indicates a similar excited-state relaxation pathway that differs from simple solvation but depends on solvent polarity, also responsible for the FQY enhancement from *o*-HBDI to *o*-LHBDI (Table 1, FQY is still well below 1). We thus surmise that the dominant P-ring-twisting events in *o*-HBDI (Figure S6b) correspond to the ultrafast "counterpart" of I-ring-twisting events in *o*-LHBDI (Figure S6d), while both isomerization pathways are sensitive to solvent polarity due to the accompanying ICT process. Notably, only target analysis yields a reasonable trace for the TICT(I) state since all states past ESIPT are spectrally similar in global analysis.[35] The slightly mismatched peak maxima between the SE band of T* FS (i.e., S_1-keto form) and steady-state fluorescence band likely arise from an overlapping ESA band on blue side of the SE band, along with the additional λ^2 dependence of the SE cross-section, thus leading to an apparent redshift of the SE peak.[10] In contrast to the proposed twisting population without undergoing ESIPT (i.e., S_1-enol form) toward a peaked S_1/S_0 conical intersection,[42] our systematic TA spectra of *o*-LHBDI in various solvents substantiate the S_1-keto form (T*) as the dominant excited-state population that relaxes toward a sloped conical intersection,[41] while generating enhanced fluorescence due to kinetic trapping of the FS.[10,45] A long-lived ground state recovery of *o*-LHBDI's N-form on the μs timescale is expected on the basis of the aforementioned recovery dynamics of *o*-HBDI in ACN.[30]

2.3. Ground and Excited-State Femtosecond Stimulated Raman Spectroscopy (FSRS) Affords Structural Dynamics Insights. To correlate the electron motions with molecular

vibrations in real time, we implemented ground- and excited-state FSRS in tandem to gain structural dynamics insights of the comparative *o*-HBDI and *o*-LHBDI, including their respective normal and tautomer forms. The ground-state FSRS data were obtained using a 506 nm Raman pump with a bluer Raman probe to achieve pre-resonance condition at the red edge of the N-form absorption (Figure 1) and highlight its vibrational features. In contrast, the excited-state FSRS employed a 545 nm Raman pump with a redder Raman probe (plus a 400 nm actinic pump) to achieve pre-resonance on the blue (red) edge of the N (T)-form's ESA band (Figures 3 and 4).[10] This Raman pump wavelength was strategically tuned to a "central" region between the positive ESA and negative SE peaks,[35] which can enhance the signal-to-noise ratios of transient N* and T* forms of both chromophores to allow for the dynamic tracking and rigorous comparison of vibrational signatures throughout ESIPT (see SI Experimental Materials and Methods for details).

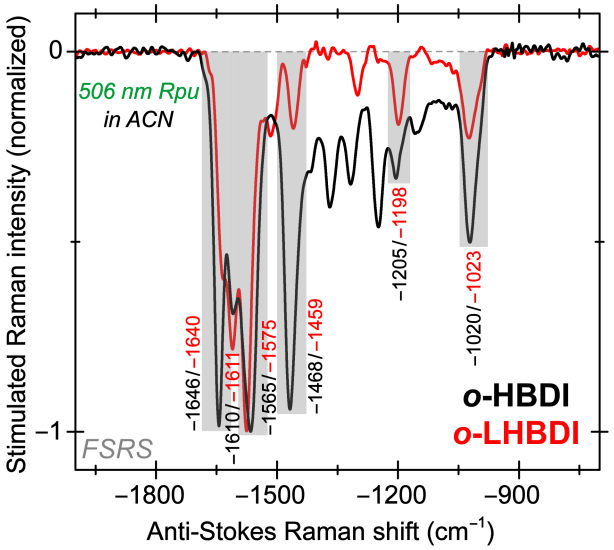

Figure 5. Ground-state FSRS reveals key structural features of *o*-HBDI (black) and *o*-LHBDI (red) in ACN. Raman pump was tuned to 506 nm with Raman probe on the anti-Stokes side. The stimulated Raman intensity is normalized to the ~1570 cm^{-1} peak. Major Raman peak frequency shifts upon P-ring locking (gray shades) are color-coded according to the chromophore (see Table S2 for vibrational normal mode assignments). R_{pu}, Raman pump.

The ground-state FSRS spectra of the N-forms of *o*-HBDI and *o*-LHBDI in ACN show largely conserved vibrational bands ranging from ~1000–1700 cm^{-1} (Figure 5) with mode assignments aided by quantum calculations (Table S2). Overall, lower-frequency modes are more delocalized vibrations like ring deformation, while higher-frequency modes involve more localized CO, CN, and CC stretching motions.[10] The Raman mode assignments are largely consistent with previous reports on *p*-HBDI,[22,46] particularly on the I ring, due to the structurally similar backbone of the constitutional isomer. The P-ring locking modifies the conjugation and alters the overall electronic and atomic structure of *o*-LHBDI, which becomes apparent in frequency shifts (see Table S2 for summary) and intensity variation of multiple Raman peaks, the latter probing the mode-dependent polarizability change of the chromophore (Figure 5). For instance, the significant drop of ~1460 and 1640 cm^{-1} peak intensities in *o*-LHBDI stems from the P-ring locking (with extra ring, Scheme 2) that increases electron density and decreases electron deformability for the P-ring-dominant motions, whereas the ~1610 cm^{-1} peak intensity remains nearly constant due to its primary P- and I-ring contribution in *o*-HBDI and *o*-LHBDI, respectively (see Table S2 for mode assignments).

The excited-state FSRS for *o*-HBDI and *o*-LHBDI following 400 nm photoexcitation of N-forms yields spectrally similar trends (Figure 6a and d). The different signs of Raman marker bands arise from the specific resonance condition ("+/–" for initial N* modes above/below 1500 cm^{-1}) or transient species ("+" for a nascent T* mode around 560 cm^{-1}).[10,35] The N* vibrational modes with P-ring-dominant motions red-shift while I-ring-dominant motions blue-shift versus the ground state (Tables S3 and S4), indicative of an ICT process[10,23] that underlies the solvent-polarity dependence revealed by systematic TA experiments (see Section 2.2). All the excited-state modes display a blueshift over time, denoting vibrational relaxation of transient species,[10,45] with the 1579 cm^{-1} mode having the most significant shift (see black arrow in Figure 6a). Both high-frequency

modes at 1579 and 1669 cm^{-1} reflect rather delocalized vibrational motions in S_0 (~1610 and 1646 cm^{-1}, Table S2) that become more localized to P-ring (N*) or I-ring (T*) motions in S_1 (Table S3), likely due to a photoinduced swift electronic charge redistribution, ESIPT, and ICT[22,29,30] that enable the chromophore to undergo an ultrafast twist dominantly along one bridge bond, P ring in *o*-HBDI and I ring in *o*-HBDI, but not both simultaneously to break the two-ring coplanarity.

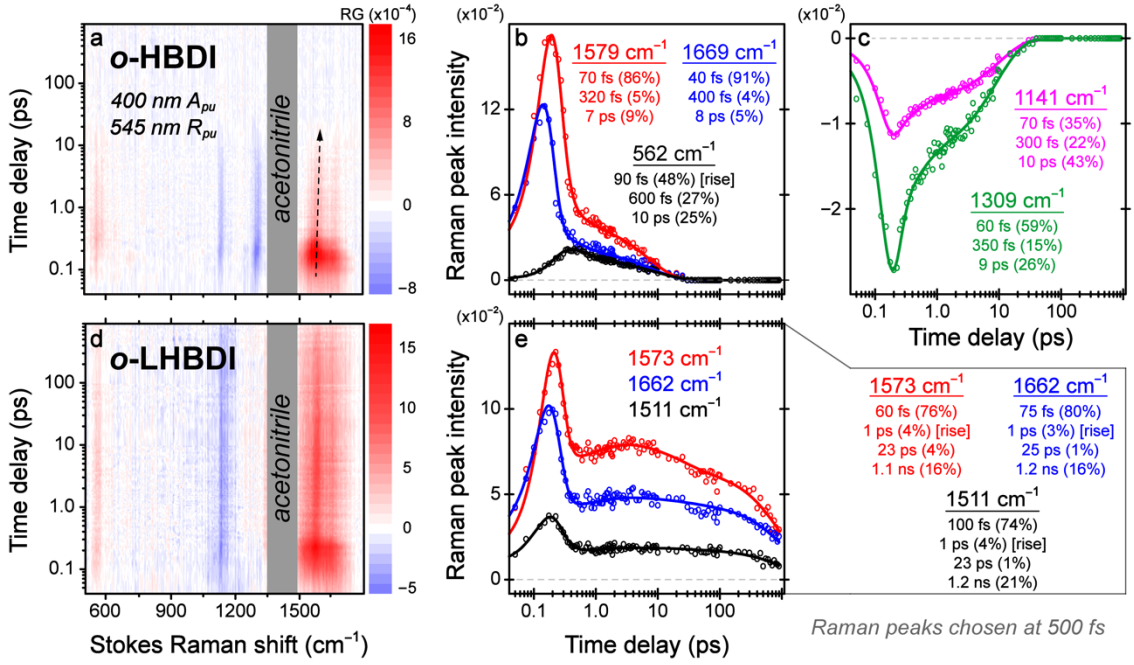

Figure 6. Excited-state FSRS tracks structural dynamics in real time. The semilogarithmic 2D-contour plots of the excited-state FSRS data after 400 nm excitation of (a) *o*-HBDI and (d) *o*-LHBDI in ACN. Raman pump was tuned to 545 nm with a probe window of ~500–1800 cm^{-1} on the Stokes side. The stimulated Raman gain (RG) color bar is displayed. The integrated intensity dynamics (data in hollow circles) of the positive (b) 562, 1579, and 1669 cm^{-1} and negative (c) 1309 and 1141 cm^{-1} Raman bands of *o*-HBDI and positive (e) 1511, 1573, and 1662 cm^{-1} Raman bands of *o*-LHBDI in ACN are overlaid with least-squares fits (color-coded solid lines). The retrieved time constants and amplitude weight percentages are listed in the insets. A_{pu}, actinic pump; R_{pu}, Raman pump.

The intensity dynamics of five (three) pronounced excited-state vibrational modes in *o*-HBDI (*o*-LHBDI) largely match the fs-TA results (Figure 6b, c, e, and Figures 3, 4); therefore, they track similar excited-state processes. Importantly, the <100 fs time constant representing ESIPT from N*→T* manifests a decay for all the vibrational modes except the ~562 cm^{-1} mode in *o*-HBDI, wherein a rise component was observed. Clear dynamics were not obtained for the ~556 cm^{-1} mode in *o*-LHBDI, possibly due to the weaker mode intensity (supported by calculations in Figure S7). This mode tracks P-ring deformation motions that can modulate the O–H···N distance and is likely a spectator mode for ESIPT.[10,15] Therefore, while most of the excited-state modes follow the decay of N* species in *o*-HBDI, the 562 cm^{-1} mode tracks the rise of T* species and subsequent decay. Though this mode was absent in ground-state FSRS (Figure 5), the calculated ground-state Raman spectra of *o*-HBDI and *o*-LHBDI in ACN show enhanced Raman intensity for this mode in the tautomer form (Figure S7), supporting its direct involvement with ESIPT. The close match between the initial decay (40–70 fs) and rise (90 fs) time constants (Figure 6b,c) from multiple vibrational modes establishes the real-time tracking of ESIPT in action, which represents the first-time experimental observation for *ortho*-GFP-chromophore analogues in solution.

Notably, a conserved ~1 ps rise component was retrieved for the high-frequency modes in *o*-LHBDI (Figure 6e), which was not observed for *o*-HBDI (Figure 6b). This intermediate rise time constant largely matches the solvation time of ACN and could result from the increased electric polarizability as the P-ring-locked chromophore becomes solvated upon N*→T* electron density redistribution en route to the FS (Figure 4, kinetic scheme),[47] which is more significant with larger time constants than the more conformationally flexible *o*-HBDI (Figure 3, kinetic scheme). It should be noted that the ground-state T-form relaxation (>ns) in *o*-HBDI retrieved from fs-TA was not observed in the excited-state FSRS peak dynamics due to a change in the polarizability and

resonance conditions, since the dynamic resonance enhancement was achieved for excited-state species (N* and T*) in accord with their transient electronic features (Figure 3).[10] In contrast, for *o*-LHBDI with an altered excited-state relaxation pathway that leads to a twisted dark state and more emissive FS (than *o*-HBDI), the T*-form electronic relaxation time constants of ~15 ps and 1.2 ns (Figure 4d) in ACN are well corroborated by the T* vibrational mode intensity decay time constants of ~24 ps and 1.2 ns (Figure 6e), inferring the correlated electronic and atomic motions.

2.4. ESIPT and Isomerization Coordinates Elucidated for Constraining the *ortho*-GFP-Chromophore in Solution. The ground and excited state measurements in the electronic and vibrational domains, validated by quantum calculations, support the occurrence of ESIPT from the neutral P-ring unlocked and locked *ortho*-GFP chromophore derivatives in solvents with various properties (e.g., polarity, viscosity). The formation of a seven-membered-ring intramolecular H-bond in the *ortho*-isomer facilitates the otherwise-inhibited proton transfer as observed in the *para*-isomer that is outcompeted by ultrafast *cis*-*trans* isomerization.[21,22,32,33] The change in the excited-state PES upon P-ring locking initially becomes apparent from the solvent-polarity dependent emission energies (Figures 1 and S2, Table 1). The emission energies are largely conserved for *o*-HBDI, suggesting that the planar T* FS occurs before the solvation and isomerization events that would be more sensitive to solvent polarity. In contrast, a frequency blueshift is apparent for *o*-LHBDI as the solvent varies from polar protic to nonpolar aprotic (MeOH to Tol, see Figure S2e), insinuating that solvation events play a more significant role in the excited state of the locked chromophore. As corroboration, the FQY of *o*-LHBDI also displays a stronger correlation with solvent polarity than the unlocked *o*-HBDI (Figure 2a,c). We note that the observation of only the zwitterionic form (T*, see Schemes 1 and 2) emission in steady-state fluorescence spectrum (Figure 1, corroborated by the *o*-HBDI anionic form emission spectrum in Figure S4) as well as

ultrafast formation of the zwitterionic form (T*, Figures 3 and 4) in fs-TA spectra indicates that the ESIPT efficiency is not dramatically decreased for these *ortho*-GFP chromophores (both *o*-HBDI and *o*-LHBDI) in protic solvents like MeOH.

Furthermore, the evidence denoting an altered excited-state PES upon P-ring locking arises from the solvent-viscosity dependent FQY enhancement from *o*-HBDI to *o*-LHBDI as one of the two key isomerization coordinates is isolated (Figure 2f). The much greater FQY enhancement in the lower viscosity solvents (ACN > DCM > MeOH > Tol, see their η values in Table 1) provides strong experimental support for P-ring isomerization as the dominant pathway for nonradiative relaxation (likely via a CI)[38,41,42,45] because the two *ortho*-GFP chromophores only differ in the extra ring (i.e., five-membered ring cyclization, Scheme 2) that inhibits the one-bond-flip of P ring while I-ring isomerization remains accessible.

By implementing fs-TA spectroscopy and analyzing time-resolved electronic features, the ESIPT from N*→T* was confirmed to be ultrafast (<100 fs) for both chromophores in all solvents, including MeOH. The barrierless ESIPT reaction was experimentally supported by fs fluorescence upconversion results: deuteration of the P-ring hydroxy group does not alter the rise and decay dynamics of the tautomer emission band.[13,36] Theoretical studies of *o*-HBDI and *o*-LHBDI also concluded that ultrafast (<35 fs), barrierless ESIPT precedes the competing isomerization events and is unaffected by the P-ring locking.[38,41,42] This finding suggests that the increased photoacidity of the phenolic hydroxy group from N→N* is not drastically affected by changes in the electronic structure upon P-ring locking (Figure S3 and Table S1), while post ultrafast ESIPT, the phenolate oxygen site with an enhanced electron-donating capability leads to ICT toward I ring (Table S1) and the structural reorganization plays a more prominent role in that phase of energy relaxation (Figure 6).[13]

Notably, intermolecular H-bonding between the solute and solvent can compete with ESIPT and decrease the tautomerization efficiency.[11,12,40] For polar solvents with H-bond donating and/or accepting capabilities (e.g., MeOH and ACN), ESIPT can be hindered such that N* rapidly relaxes back to the ground state through internal conversion or conical intersection without detectable N* emission and in turns lowers the FQY of T*. The effect of solvent polarity on transient electronic dynamics of both *o*-HBDI and *o*-LHBDI (Figures 3 and 4) can be unveiled by the excited-state relaxation rate constant versus solvent polarity plots (Figure S6). Since we have experimentally established that P-ring isomerization is dominant and responsible for majority of the nonradiative energy dissipation, we can dissect solvent effects on the I-ring isomerization pathway. Although the FQY increases by a factor of ~18 (15) in *o*-HBDI (*o*-LHBDI) from MeOH to Tol (Table 1), we select *o*-LHBDI with an isolated bridge-twisting coordinate to examine solvent-induced effects on I-ring isomerization of T* species with an increased polarity versus N*. Therefore, the more polar solvents can lower the T* energy and reduce the energy barrier for TICT(I),[31] effectively red-shifting the emission and lowering the FQY. On the contrary, Tol is unable to stabilize T* as efficiently and raises the energy barrier for TICT(I), resulting in a bluer emission energy and a higher FQY. Notably, such insights augment the original proposal[13] that I-ring twist is originally restricted by the intramolecular hydrogen bond, and after ultrafast ESIPT, the I-ring isomerization pathway is opened in the excited state of *o*-LHBDI and contributes to its overall FQY (Table 1).

Due to our <1 ns time window in fs-TA, the long-lived (μs) ground-state *trans*-T relaxation[30] for *o*-HBDI in ACN was not observed. The estimated <5% population of *trans*-T form[30] would yield an extremely low and essentially negligible amplitude if added to our global and target analysis models. Rather, we focused on ESIPT and the subsequent excited- and ground-state decay dynamics of *cis*-T* and the partially twisted *cis*-T that prominently emerges on the tens of ps

timescale in solution (Figure 3). Theoretical studies of the T→N reverse proton transfer was also determined to be largely downhill, as corroborated by our quantum calculations in the ground state with a small barrier around P-ring O–H bond distance of 1.4 Å (Figure S1a), thus supporting the few-ns relaxation phase of the twisted *cis*-T species to be a meaningful assignment in *o*-HBDI.[38,41]

Moreover, the ground- and excited-state FSRS results complement the findings from steady-state and time-resolved electronic spectroscopy experiments to create a holistic understanding of the reaction coordinates of both *ortho*-GFP chromophore analogues. Upon photoexcitation, the P-ring-dominant vibrational mode frequency redshift from N→N* is consistent with electron density redistribution and increased photoacidity of the phenolic hydroxy group to promote ESIPT (Tables S3 and S4).[9,11,12] The concomitant blueshift for the I-ring-dominant vibrational modes suggests the P-to-I-ring ICT, which can be further categorized as the ESIPT-coupled ICT since the phenolic hydroxy group is a weak electron donor unless it is deprotonated.[23,29] This assignment is augmented by the predicted blueshift (redshift) of the I-ring (P-ring)-dominant vibrational modes for N*→T* transition from quantum calculations (Tables S3 and S4), while a direct experimental observation is hindered due to the ultrafast emergence of T* species after ESIPT reaction (<100 fs). In particular, the ~1669 (1662) cm^{-1} excited-state vibrational mode in *o*-HBDI (*o*-LHBDI) mainly consists of the characteristic I-ring C=O stretch, along with CNH rocking, which could thus act as a direct P-to-I-ring ICT probe since it is clearly blue-shifted from the ground state (Figures 5 and 6). Like *p*-HBDI, P-to-I-ring ICT could contribute to the enhanced P-ring isomerization to rapidly dissipate the excited state energy.[21,22,33,39,44,48] The higher polarity solvents stabilize T*, lower the excited-state isomerization barriers, and enhance P-to-I-ring ICT and the subsequent P-ring isomerization (mainly for *o*-HBDI), ultimately leading to the lower FQYs as observed for both chromophores in MeOH and ACN than those in DCM and Tol (see Table 1).

Notably for the first time, the ultrafast (<100 fs) ESIPT process was captured in *o*-HBDI using FSRS, aided by dynamic resonance enhancement.[7,10,35] The rise of ~562 cm^{-1} mode, tracking the characteristic P-ring deformation motions that modulate the O–H···N (intramolecular H-bond) distance, appears later in time than all the other modes that rise within the cross-correlation time (Figure 6a-c). We attribute the sub-100 fs decay and rise components in the other excited-state vibrational modes and ~562 cm^{-1} mode to photoreactant N* and photoproduct T*, respectively. Further support arose from previous fluorescence upconversion measurements of T* showing two coherently excited skeletal deformation motions (~115 and 236 cm^{-1}) in association with the intramolecular hydrogen bond.[30] These results infer a moderate energy barrier for ESIPT that can be overcome by in-plane skeletal bending motions to modify the "interlocked" H-bond distance (Scheme 2),[11] which also correlate well with previous findings of certain low-frequency vibrational motions that effectively gate the ESPT reaction in GFP and GFP-derived biosensors,[49,50] as well as inhibition of the chromophore isomerization coordinate to enhance FQY.[10,34,35]

3. Conclusion

In summary, the conformational P-ring locking of an *ortho*-GFP derived chromophore yields a dramatic FQY enhancement that is solvent-viscosity dependent. Deeper insights into the photophysical behavior of two archetypal *ortho*-GFP-chromophore analogues in the electronic and vibrational domains were obtained using an integral characterization platform of fs-TA, excited-state FSRS, and quantum calculations. The use of contrasting solvents that cover a wide range of polarity, viscosity, and protic properties allows for a systematic investigation of excited-state energy relaxation pathways. Upon photoexcitation, ultrafast electron density redistribution leads to increased photoacidic and photobasic behavior for the P-ring hydroxy group and I-ring N site, respectively. The resultant ESIPT-induced directional ICT steers the energy dissipation pathways

along the P- and I-ring isomerization coordinates via the exocyclic methine bridge, with the former route being inhibited upon P-ring locking via cyclization. The rise of a ~562 cm^{-1} Raman mode, probing the P-ring-deformation motions that can readily modulate the O–H···N distance along the intramolecular H-bond, was captured during ESIPT reaction on the ~90 fs timescale, providing crucial structural dynamics knowledge. The ultrafast P-to-I-ring ICT facilitates P-ring twist (partial isomerization), rapidly returning the *o*-HBDI population to the ground state with essentially no fluorescence. In sharp contrast, the fluorescent state of *o*-LHBDI becomes much more sensitive to solvent polarity with the dominant P-ring isomerization coordinate inhibited, allowing us to directly observe that the I-ring twist energy barrier increases as solvent polarity decreases, resulting in a higher FQY. The higher-polarity solvents exhibit red-shifted emission as they are better suited to further stabilize the highly polar zwitterionic T* population, and a lower energy barrier leading to a dark TICT(I) population with a twisted geometry that relaxes nonradiatively to the ground state. In both chromophores, the *cis*-to-*trans* photoisomerization quantum yield remains very low due to the intramolecular hydrogen bond and additional P-ring locking in *o*-LHBDI, so the vast population of partially twisted *cis*-T species undergoes reverse proton transfer on ultrafast timescales to the thermally equilibrated *cis*-N form and complete the photocycle.

Strategic incorporation of electron-donating and -withdrawing groups at various positions on the P and I rings can provide further insights into the effect of ESIPT-induced ICT that leads to ultrafast excited state deactivation for ESIPT-capable "floppy" molecules, so long as they do not interfere with the ESIPT process that alleviates the need for extended conjugation to achieve red emission. Future endeavors of such compact-sized derivatives with rational molecular engineering (e.g., conformational locking, charge transfer direction and magnitude, site-specific synergistic tuning)[9,23] and suitable spectroscopic characterization would provide an enhanced understanding

of the substituent-position relationships behind electron density redistribution and light-induced properties with functional importance (e.g., brightness, stability, color tuning). We envision the deepened mechanistic insights into ultrafast fluorescence modulation as the root cause for emission properties to enable rational molecular design and benefit broad applications from chemical-/bio-probe development, ratiometric sensing, to super-resolution imaging and microscopy.

ACKNOWLEDGMENTS

This work was supported by the U.S. NSF grant CHE-2003550 (C.F.). The chemical synthesis part was supported by Russian Science Foundation grant No. 18-73-10105 (M.S.B.). We also appreciate the Oregon State University (OSU) Department of Chemistry Milton Harris Graduate Fellowship in Summer 2021 (S.A.B.), and thank Taylor Krueger for helpful discussions.

REFERENCES

(1) Eigen, M. Proton Transfer, Acid-Base Catalysis, and Enzymatic Hydrolysis. *Angew. Chem. Int. Ed.* **1964**, *3*, 1-72.

(2) Agmon, N.; Huppert, D.; Masad, A.; Pines, E. Excited-State Proton-Transfer to Methanol Water Mixtures. *J. Phys. Chem.* **1991**, *95*, 10407-10413.

(3) Rini, M.; Magnes, B.-Z.; Pines, E.; Nibbering, E. T. J. Real-Time Observation of Bimodal Proton Transfer in Acid-Base Pairs in Water. *Science* **2003**, *301*, 349-352.

(4) Nibbering, E. T. J.; Fidder, H.; Pines, E. Ultrafast Chemistry: Using Time-Resolved Vibrational Spectroscopy for Interrogation of Structural Dynamics. *Annu. Rev. Phys. Chem.* **2005**, *56*, 337-367.

(5) Tang, K.-C.; Chang, M.-J.; Lin, T.-Y.; Pan, H.-A.; Fang, T.-C.; Chen, K.-Y.; Hung, W.-Y.; Hsu, Y.-H.; Chou, P.-T. Fine Tuning the Energetics of Excited-State Intramolecular Proton Transfer (ESIPT): White Light Generation in A Single ESIPT System. *J. Am. Chem. Soc.* **2011**, *133*, 17738-17745.

(6) Zhao, J.; Ji, S.; Chen, Y.; Guo, H.; Yang, P. Excited State Intramolecular Proton Transfer (ESIPT): From Principal Photophysics to the Development of New Chromophores and Applications in Fluorescent Molecular Probes and Luminescent Materials. *Phys. Chem. Chem. Phys.* **2012**, *14*, 8803-8817.

(7) Liu, W.; Wang, Y.; Tang, L.; Oscar, B. G.; Zhu, L.; Fang, C. Panoramic Portrait of Primary Molecular Events Preceding Excited State Proton Transfer in Water. *Chem. Sci.* **2016**, *7*, 5484-5494.

(8) Hoffman, D. P.; Mathies, R. A. Femtosecond Stimulated Raman Exposes the Role of Vibrational Coherence in Condensed-Phase Photoreactivity. *Acc. Chem. Res.* **2016**, *49*, 616-625.

(9) Sedgwick, A. C.; Wu, L.; Han, H.-H.; Bull, S. D.; He, X.-P.; James, T. D.; Sessler, J. L.; Tang, B. Z.; Tian, H.; Yoon, J. Excited-State Intramolecular Proton-Transfer (ESIPT) Based Fluorescence Sensors and Imaging Agents. *Chem. Soc. Rev.* **2018**, *47*, 8842-8880.

(10) Fang, C.; Tang, L.; Chen, C. Unveiling Coupled Electronic and Vibrational Motions of Chromophores in Condensed Phases. *J. Chem. Phys.* **2019**, *151*, 200901.

(11) Chen, C.-L.; Chen, Y.-T.; Demchenko, A. P.; Chou, P.-T. Amino Proton Donors in Excited-State Intramolecular Proton-Transfer Reactions. *Nat. Rev. Chem.* **2018**, *2*, 131-143.

(12) Kwon, J. E.; Park, S. Y. Advanced Organic Optoelectronic Materials: Harnessing Excited-State Intramolecular Proton Transfer (ESIPT) Process. *Adv. Mater.* **2011**, *23*, 3615-3642.

(13) Hsu, Y.-H.; Chen, Y.-A.; Tseng, H.-W.; Zhang, Z.; Shen, J.-Y.; Chuang, W.-T.; Lin, T.-C.; Lee, C.-S.; Hung, W.-Y.; Hong, B.-C.; et al. Locked *ortho*- and *para*-Core Chromophores of Green Fluorescent Protein; Dramatic Emission Enhancement via Structural Constraint. *J. Am. Chem. Soc.* **2014**, *136*, 11805-11812.

(14) Padalkar, V. S.; Seki, S. Excited-State Intramolecular Proton-Transfer (ESIPT)-Inspired Solid State Emitters. *Chem. Soc. Rev.* **2016**, *45*, 169-202.

(15) Krueger, T. D.; Fang, C. Elucidating Inner Workings of Naturally Sourced Organic Optoelectronic Materials with Ultrafast Spectroscopy. *Chem. Eur. J.* **2021**, *27*, 17736–17750.

(16) Shimomura, O.; Johnson, F. H.; Saiga, Y. Extraction, Purification and Properties of Aequorin, a Bioluminescent Protein from the Luminous Hydromedusan, *Aequorea*. *J. Cell. Comp. Physiol.* **1962**, *59*, 223-239.

(17) Tsien, R. Y. The Green Fluorescent Protein. *Annu. Rev. Biochem.* **1998**, *67*, 509-544.

(18) Krueger, T. D.; Giesbers, G.; Van Court, R. C.; Zhu, L.; Kim, R.; Beaudry, C. M.; Robinson, S. C.; Ostroverkhova, O.; Fang, C. Ultrafast Dynamics and Photoresponse of a Fungi-Derived Pigment Xylindein from Solution to Thin Films. *Chem. Eur. J.* **2021**, *27*, 5627-5631.

(19) Krueger, T. D.; Solaris, J.; Tang, L.; Zhu, L.; Webber, C.; Van Court, R. C.; Robinson, S. C.; Ostroverkhova, O.; Fang, C. Illuminating Excited-State Intramolecular Proton Transfer of a Fungi-Derived Red Pigment for Sustainable Functional Materials. *J. Phys. Chem. C* **2022**, *126*, 459-477.

(20) Webber, N. M.; Litvinenko, K. L.; Meech, S. R. Radiationless Relaxation in a Synthetic Analogue of the Green Fluorescent Protein Chromophore. *J. Phys. Chem. B* **2001**, *105*, 8036-8039.

(21) Altoè, P.; Bernardi, F.; Garavelli, M.; Orlandi, G.; Negri, F. Solvent Effects on the Vibrational Activity and Photodynamics of the Green Fluorescent Protein Chromophore: A Quantum-Chemical Study. *J. Am. Chem. Soc.* **2005**, *127*, 3952-3963.

(22) Taylor, M. A.; Zhu, L.; Rozanov, N. D.; Stout, K. T.; Chen, C.; Fang, C. Delayed Vibrational Modulation of the Solvated GFP Chromophore into a Conical Intersection. *Phys. Chem. Chem. Phys.* **2019**, *21*, 9728-9739.

(23) Chen, C.; Fang, C. Devising Efficient Red-Shifting Strategies for Bioimaging: A Generalizable Donor-Acceptor Fluorophore Prototype. *Chem. Asian J.* **2020**, *15*, 1514-1523.

(24) Chatterjee, T.; Mandal, M.; Das, A.; Bhattacharyya, K.; Datta, A.; Mandal, P. K. Dual Fluorescence in GFP Chromophore Analogues: Chemical Modulation of Charge Transfer and Proton Transfer Bands. *J. Phys. Chem. B* **2016**, *120*, 3503-3510.

(25) Ni, M.; Su, S.; Fang, H. Substituent Control of Photophysical Properties for Excited-State Intramolecular Proton Transfer (ESIPT) of *o*-LHBDI Derivatives: A TD-DFT Investigation. *J. Mol. Model.* **2020**, *26*, 108.

(26) Fang, X.; Wang, Y.; Wang, D.; Zhao, G.; Zhang, W.; Ren, A.; Wang, H.; Xu, J.; Gao, B.-R.; Yang, W. Synthesized Blue Fluorescent Protein Analogue with Tunable Colors from Excited-State Intramolecular Proton Transfer through an N–H···N Hydrogen Bond. *J. Phys. Chem. Lett.* **2014**, *5*, 92-98.

(27) Alarcos, N.; Gutierrez, M.; Liras, M.; Sánchez, F.; Douhal, A. An Abnormally Slow Proton Transfer Reaction in a Simple HBO Derivative due to Ultrafast Intramolecular-Charge Transfer Events. *Phys. Chem. Chem. Phys.* **2015**, *17*, 16257-16269.

(28) Chen, K.-Y.; Hsieh, C.-C.; Cheng, Y.-M.; Lai, C.-H.; Chou, P.-T. Extensive Spectral Tuning of the Proton Transfer Emission from 550 to 675 nm via a Rational Derivatization of 10-Hydroxybenzo[h]quinoline. *Chem. Commun.* **2006**, *2006*, 4395-4397.

(29) Demchenko, A. P.; Tang, K.-C.; Chou, P.-T. Excited-State Proton Coupled Charge Transfer Modulated by Molecular Structure and Media Polarization. *Chem. Soc. Rev.* **2013**, *42*, 1379-1408.

(30) Hsieh, C.-C.; Chou, P.-T.; Shih, C.-W.; Chuang, W.-T.; Chung, M.-W.; Lee, J.; Joo, T. Comprehensive Studies on an Overall Proton Transfer Cycle of the *ortho*-Green Fluorescent Protein Chromophore. *J. Am. Chem. Soc.* **2011**, *133*, 2932-2943.

(31) Chen, C.; Boulanger, S. A.; Sokolov, A. I.; Baranov, M. S.; Fang, C. A Novel Dialkylamino GFP Chromophore as an Environment-Polarity Sensor Reveals the Role of Twisted Intramolecular Charge Transfer. *Chemosensors* **2021**, *9*, 234.

(32) Mandal, D.; Tahara, T.; Meech, S. R. Excited-State Dynamics in the Green Fluorescent Protein Chromophore. *J. Phys. Chem. B* **2004**, *108*, 1102-1108.

(33) Gepshtein, R.; Huppert, D.; Agmon, N. Deactivation Mechanism of the Green Fluorescent Chromophore. *J. Phys. Chem. B* **2006**, *110*, 4434-4442.

(34) Baranov, M. S.; Lukyanov, K. A.; Borissova, A. O.; Shamir, J.; Kosenkov, D.; Slipchenko, L. V.; Tolbert, L. M.; Yampolsky, I. V.; Solntsev, K. M. Conformationally Locked Chromophores as Models of Excited-State Proton Transfer in Fluorescent Proteins. *J. Am. Chem. Soc.* **2012**, *134*, 6025-6032.

(35) Chen, C.; Liu, W.; Baranov, M. S.; Baleeva, N. S.; Yampolsky, I. V.; Zhu, L.; Wang, Y.; Shamir, A.; Solntsev, K. M.; Fang, C. Unveiling Structural Motions of a Highly Fluorescent

Superphotoacid by Locking and Fluorinating the GFP Chromophore in Solution. *J. Phys. Chem. Lett.* **2017**, *8*, 5921–5928.

(36) Chen, K.-Y.; Cheng, Y.-M.; Lai, C.-H.; Hsu, C.-C.; Ho, M.-L.; Lee, G.-H.; Chou, P.-T. Ortho Green Fluorescence Protein Synthetic Chromophore; Excited-State Intramolecular Proton Transfer via a Seven-Membered-Ring Hydrogen-Bonding System. *J. Am. Chem. Soc.* **2007**, *129*, 4534-4535.

(37) Reichardt, C.; Welton, T. *Solvents and Solvent Effects in Organic Chemistry*, 4th ed.; Wiley-VCH Verlag GmbH & Co. KGaA: Weinheim, Germany, 2011.

(38) Cui, G.; Lan, Z.; Thiel, W. Intramolecular Hydrogen Bonding Plays a Crucial Role in the Photophysics and Photochemistry of the GFP Chromophore. *J. Am. Chem. Soc.* **2012**, *134*, 1662-1672.

(39) Boulanger, S. A.; Chen, C.; Tang, L.; Zhu, L.; Baleeva, N. S.; Myasnyanko, I. N.; Baranov, M. S.; Fang, C. Shedding Light on Ultrafast Ring-Twisting Pathways of Halogenated GFP Chromophores from the Excited to Ground State. *Phys. Chem. Chem. Phys.* **2021**, *23*, 14636-14648.

(40) Li, Y.; Yang, Y.; Ding, Y. The New Competitive Mechanism of Hydrogen Bonding Interactions and Transition Process for the Hydroxyphenyl Imidazo [1, 2-a] Pyridine in Mixed Liquid Solution. *Sci. Rep.* **2017**, *7*, 1574.

(41) Ai, Y.-J.; Liao, R.-Z.; Fang, W.-H.; Luo, Y. Theoretical Studies on the Isomerization Mechanism of the *ortho*-Green Fluorescent Protein Chromophore. *Phys. Chem. Chem. Phys.* **2012**, *14*, 13409-13414.

(42) Liu, X.-Y.; Chang, X.-P.; Xia, S.-H.; Cui, G.; Thiel, W. Excited-State Proton-Transfer-Induced Trapping Enhances the Fluorescence Emission of a Locked GFP Chromophore. *J. Chem. Theory Comput.* **2016**, *12*, 753-764.

(43) Snellenburg, J. J.; Laptenok, S. P.; Seger, R.; Mullen, K. M.; van Stokkum, I. H. M. Glotaran: A Java-Based Graphical User Interface for the R-Package TIMP. *J. Stat. Softw.* **2012**, *49*, 1-22.

(44) Jones, C. M.; List, N. H.; Martínez, T. J. Resolving the Ultrafast Dynamics of the Anionic Green Fluorescent Protein Chromophore in Water. *Chem. Sci.* **2021**, *12*, 11347-11363.

(45) Kumpulainen, T.; Lang, B.; Rosspeintner, A.; Vauthey, E. Ultrafast Elementary Photochemical Processes of Organic Molecules in Liquid Solution. *Chem. Rev.* **2017**, *117*, 10826-10939.

(46) Esposito, A. P.; Schellenberg, P.; Parson, W. W.; Reid, P. J. Vibrational Spectroscopy and Mode Assignments for an Analog of the Green Fluorescent Protein Chromophore. *J. Mol. Struct.* **2001**, *569*, 25-41.

(47) Maroncelli, M. Computer Simulations of Solvation Dynamics in Acetonitrile. *J. Chem. Phys.* **1991**, *94*, 2084-2103.

(48) Park, J. W.; Shiozaki, T. On-the-Fly CASPT2 Surface-Hopping Dynamics. *J. Chem. Theory Comput.* **2017**, *13*, 3676-3683.

(49) Fang, C.; Frontiera, R. R.; Tran, R.; Mathies, R. A. Mapping GFP Structure Evolution During Proton Transfer with Femtosecond Raman Spectroscopy. *Nature* **2009**, *462*, 200-204.

(50) Oscar, B. G.; Liu, W.; Zhao, Y.; Tang, L.; Wang, Y.; Campbell, R. E.; Fang, C. Excited-State Structural Dynamics of a Dual-Emission Calmodulin-Green Fluorescent Protein Sensor for Calcium Ion Imaging. *Proc. Natl. Acad. Sci. U. S. A.* **2014**, *111*, 10191-10196.

Table of Contents (TOC) Graphic